

A Magnetically Transduced Whisker for Angular Displacement and Moment Sensing

Suhan Kim, Camilo Velez, Dinesh K. Patel, and Sarah Bergbreiter

Abstract—This work presents the design, modeling, and fabrication of a whisker-like sensor capable of measuring the whisker’s angular displacement as well as the applied moments at the base of the whisker. The sensor takes advantage of readily accessible and low-cost 3D magnetic sensors to transduce whisker deflections, and a planar serpentine spring structure at the whisker base is used to provide a mechanical suspension for the whisker to rotate. The sensor prototype was characterized, calibrated, and compared with analytical models of the spring system and the magnetic field. The prototype showed a moment sensing range of 1.1N·mm when deflected up to 19.7°. The sensitivity of the sensor was 0.38°/LSB for the angular displacement sensing, and 0.021 Nmm/LSB for the moment sensing. A fully integrated system is demonstrated to display real-time information from the whisker on a graphical interface.

I. INTRODUCTION

An interesting common feature in rodents is the whiskers, which can move actively and sense contact or flow simultaneously [1]. Whisker contact sensing is one of these animals’ most impressive sensing mechanisms, with the ability to sense the location [2], [3], [4], shape [5], [6], and even the texture [7] of nearby objects. Whiskers can also detect fluid flow direction in confined spaces [7], [8], [9]. These abilities are also advantageous on robots, with several previous systems employing whisker sensors (e.g., [10], [11], [12], [13], [14]).

When contact occurs between the whisker and an object in biological systems, a reaction force from the object is transmitted through the whisker body to the base, or follicle. As the follicle deforms, the contact is detected by embedded mechanoreceptors [15] which convert the deformation into neural signals. In 3D space, there are three forces and three moments applied to the follicle by the whisker. However, previous work has shown that measurement of the moments at the follicle are particularly important for detecting contact point along the whisker [16], [17]. For this reason, an important goal of the sensor in this work is to detect the applied moments at the base of the whisker, and to do so in a manner that is compact and easily scalable to arrays of whiskers.

There have been many previous approaches to whisker sensing, including both active (motorized) and passive sensors. For this work, we are primarily interested in the passive component of the sensing. One common approach is the use

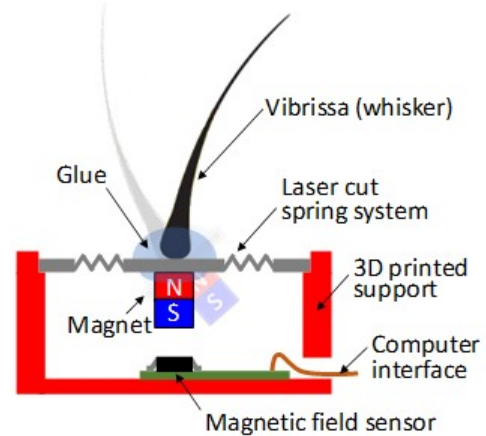


Fig. 1. Whisker sensing mechanism schematic. The whisker and a permanent magnet are glued to a mechanical suspension and the magnetic field sensor beneath the magnet is connected to a computer interface.

of four resistive strain gauges at the bottom of the whisker to measure the follicle deformation [10], [18], [19]. Similar approaches utilized load cells for transduction [20], [21]. A common structural feature of all of these approaches is that they confine the deflection of the follicle to very small strains (thereby reducing sensitivity), and are generally either large ($> 5x$ a typical rat whisker follicle) or challenging to construct and scale.

Instead, we propose a magnetic transduction approach based on easily available and low cost 3D magnetic sensor ICs (e.g., TLE493D from Infineon). The IC itself is small (footprint of 2.5 mm x 2.9 mm), uses a common I2C interface, and measures the 3D magnetic field providing information on the orientation of a magnet in 3D space. A similar transduction method has been applied to tactile sensing and integrated onto a robot hand [22]. In combination with a mechanical suspension, this approach can achieve high moment and angular deflection resolution in a very easy to construct and simple to use system. Because the magnet and suspension require no electrical connections, the entire sensing system can also be easily waterproofed for operation in air or water.

The primary contribution of this paper is the design and demonstration of this magnetic transduction approach for whisker sensing. Importantly, this experimental approach is complemented by the contribution of a combined analytical model of both the mechanical suspension and magnetic field. This model can ultimately be used for a va-

This research effort was supported by the National Science Foundation (NSF) award number BCS-1921251

The authors are with the Department of Mechanical Engineering, Carnegie Mellon University, Pittsburgh, PA, USA. Corresponding author: Sarah Bergbreiter (sbergbre@andrew.cmu.edu)

riety of mechanosensors (e.g., tactile, pressure) well beyond whiskers. The model also contributes an ability to design whisker sensors based on the range and resolution required by a specific robotic application. To validate the model and demonstrate the approach, a single whisker sensor is characterized and calibrated. A fully integrated system is demonstrated to display real-time information from the whisker on a graphical interface at 50 Hz.

II. MATERIALS AND METHODS

A. Concept

Figures 1 and 2 depict the whisker sensory system concept. The system consists of a mechanical suspension with four planar serpentine springs, a whisker, a magnet below the spring, and the 3D magnetic sensor on a printed circuit board beneath the suspension. The whisker is placed on the top surface of the serpentine spring system (chosen for low stiffness), and the magnet is attached by aligning the magnetized direction coaxial to the whisker. Movement of the whisker results in rotation and translation of the magnet, and the resulting change in magnetic field can be measured by the magnetic sensor. Therefore, moments at the whisker base can be calculated using the known mechanical stiffness of the spring system along with the angular deflection of the whisker. Angular deflection of the whisker can be determined by changes in the magnetic field from the relative position of the magnet and sensor.

B. Design and Modeling

1) *Spring system analysis:* To model the expected whisker sensor response, the first step is to understand how whisker rotations translate to forces and moments. The mechanical stiffness of a serpentine spring has been previously studied by disassembling the spring into straight beam elements [23]. By applying Castigliano's method, three external loads can be related to corresponding deflections as shown in Figure 3 and Equation 1.

$$\begin{bmatrix} \theta_0 \\ \phi_0 \\ \delta_z \end{bmatrix} = \mathbf{C} \cdot \begin{bmatrix} M_0 \\ T_0 \\ F_z \end{bmatrix} = \begin{bmatrix} C_{11} & C_{12} & C_{13} \\ C_{21} & C_{22} & C_{23} \\ C_{31} & C_{32} & C_{33} \end{bmatrix} \begin{bmatrix} M_0 \\ T_0 \\ F_z \end{bmatrix} \quad (1)$$

The compliance matrix coefficients are defined as,

$$\begin{aligned} C_{11} &= \frac{8p}{EI_a} + \frac{6l}{GJ_b}, C_{12} = C_{21} = C_{23} = C_{32} = 0 \\ C_{13} = C_{31} &= -\frac{32p^2}{EI_a} - \frac{48lp}{GJ_b}, C_{22} = \frac{8p}{GJ_a} + \frac{13l}{EI_b} \\ C_{33} &= \frac{512p^3}{3EI_a} + \frac{6l^2}{GJ_a} + \frac{4l^3}{EI_b} + \frac{230l}{GJ_b} \end{aligned}$$

Here, I_a, I_b are the vertical and horizontal moments of inertia of a spring beam, J_a, J_b are vertical and horizontal torsional constants of the cross-section of the serpentine spring beams, p is the spring's pitch, and l is half the length of a full length segment. These quantities are visualized in Figure 3. E and G are the Young's modulus and shear modulus of the spring material.

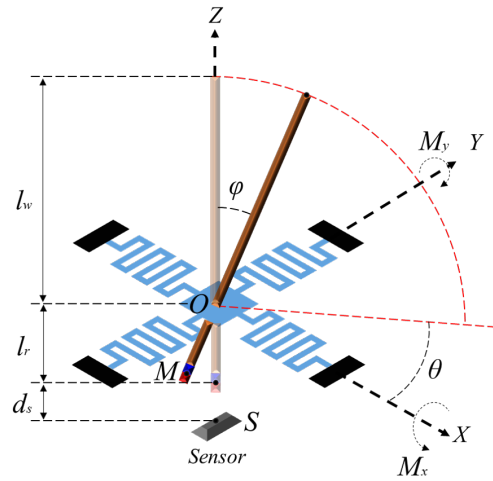


Fig. 2. Mechanical model of the whisker sensing system with modeling parameters.

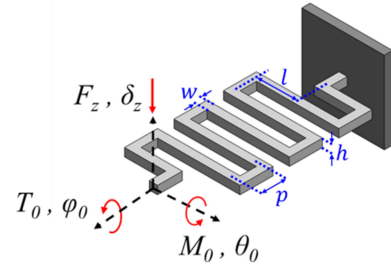


Fig. 3. Mechanical model of a serpentine spring system with dimension variables.

By tracking the equivalent bending and torsional angle of each serpentine spring, the moment applied to the center of the serpentine spring system, O (see Figure 2), in the X and Y direction can be derived. To simplify the kinematic model, an assumption was made that the base, O , rotates only and does not translate. The result is as follows.

$$\begin{bmatrix} M_x \\ M_y \end{bmatrix} = \begin{bmatrix} 0 & 2 \\ 2 & 0 \\ 0 & l \\ 2 & 0 \\ 0 & 2 \\ l & 0 \end{bmatrix}^T \begin{bmatrix} C_{12}^{-1} & C_{11}^{-1} & C_{13}^{-1} & 0 \\ C_{22}^{-1} & C_{21}^{-1} & C_{23}^{-1} & 0 \\ C_{32}^{-1} & C_{31}^{-1} & C_{33}^{-1} & 0 \\ C_{11}^{-1} & C_{12}^{-1} & 0 & C_{13}^{-1} \\ C_{21}^{-1} & C_{22}^{-1} & 0 & C_{23}^{-1} \\ C_{31}^{-1} & C_{32}^{-1} & 0 & C_{33}^{-1} \end{bmatrix} \begin{bmatrix} \theta_x \\ \theta_y \\ \delta_{z,x} \\ \delta_{z,y} \end{bmatrix} \quad (2)$$

C_{ij}^{-1} is i, j -th component of the inverse matrix of \mathbf{C} , θ_x and θ_y are rotated angle of whisker in X and Y direction, and $\delta_{z,x}$, $\delta_{z,y}$ are Z directional displacement of the spring tips (anchoring point to the center plate), that lay in X axis and Y axis respectively. Following is the result of the derivation of these displacement values.

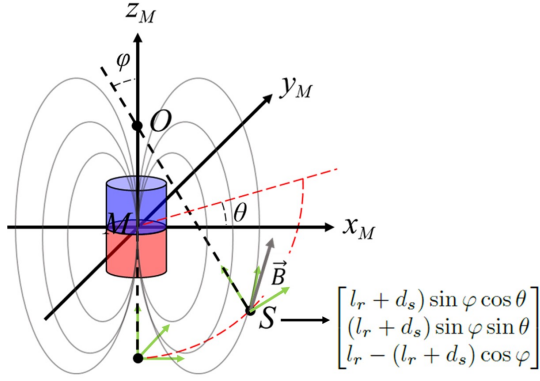


Fig. 4. The magnetic field model indicating the relative position of the sensing point with respect to the magnet-centered coordinate along with other relevant variables.

$$\begin{aligned} \theta_x &= \arcsin \left(\frac{\sin \varphi \sin \theta}{\sqrt{(\sin \varphi \sin \theta)^2 + (\cos \varphi)^2}} \right) \\ \theta_y &= \arcsin \left(\frac{\sin \varphi \cos \theta}{\sqrt{(\sin \varphi \cos \theta)^2 + (\cos \varphi)^2}} \right) \\ \delta_{z,x} &= l \cdot \cos \theta \sin \varphi \\ \delta_{z,y} &= l \cdot \sin \theta \sin \varphi \end{aligned}$$

2) *Magnetic field modeling*: The second step in modeling is to calculate how changes in the magnet position or choice of magnet relate to the measured 3-axis magnetic field (Figure 4). Assuming a cylindrical magnet, Derby and Olbert's cylindrical magnet equation [24] can be used to calculate the magnetic field vector at the sensing point if the origin of the magnet, M is known. For simplicity, this complex relationship (see Appendix) is represented as a function f_B of the sensing point S (relative to the magnet origin M), along with the magnet radius, half length, and magnetization (R , L , and M_S respectively). Note that S changes as the magnet/whisker rotates and is defined in Figure 4.

$$[B_x, B_y, B_z]_{(M)}^T = f_B \left([X_S, Y_S, Z_S]_{(M)}, R, L, M_S \right) \quad (3)$$

However, since the magnetic field is actually measured relative to the fixed coordinate frame of the sensor, a rotation matrix \mathbf{R} is required for the coordinate transformation from magnet to sensor coordinates.

$$\begin{bmatrix} B_x \\ B_y \\ B_z \end{bmatrix}_{(S)} = \mathbf{R} \cdot \begin{bmatrix} B_x \\ B_y \\ B_z \end{bmatrix}_{(M)} \quad (4)$$

The rotation matrix \mathbf{R} is defined as,

$$\mathbf{R} = \begin{bmatrix} 1 - 2 \sin^2 \frac{\varphi}{2} \cos^2 \theta & -2 \sin^2 \frac{\varphi}{2} \cos \theta \sin \theta & -\sin \varphi \cos \theta \\ -2 \sin^2 \frac{\varphi}{2} \cos \theta \sin \theta & 1 - 2 \sin^2 \frac{\varphi}{2} \sin^2 \theta & -\sin \varphi \sin \theta \\ \sin \varphi \cos \theta & \sin \varphi \sin \theta & 1 - 2 \sin^2 \frac{\varphi}{2} \end{bmatrix}$$

3) *Design parameters*: Actual design parameters for the fabricated whisker sensor are provided in Table I. Symbols can be found in Figures 2, 3, and 4. The remanent magnetization of the N50 magnet used was calculated from an N50 magnet characterization curve, and substituted as magnetization M_S in Table I.

TABLE I

WHISKER SENSOR PARAMETERS, SYMBOLS, AND DESIGNED VALUES

Parameter	Symbol	Value	Unit
Length of whisker	l_w	55	mm
Length of root	l_r	1	mm
Distance from magnet center to sensor	d_s	2.45	mm
Width of serpentine spring beams	w	100	μm
Lateral beam length of serpentine spring	$2l$	1000	μm
Pitch between lateral beams	p	300	μm
Thickness of serpentine spring	h	100	μm
Young's Modulus of serpentine spring	E	200	GPa
Shear Modulus of serpentine spring	G	77.2	GPa
Radius of magnet	R	0.5	mm
Height of magnet	$2L$	2	mm
Magnetization	M_S	1073.4	kA/m

C. Fabrication

The serpentine spring suspension was fabricated by laser cutting a 100 μm thick stainless steel sheet. An LPFK UV laser cutter was used with an optimized cutting recipe (1.5 W power, 65 repetitions), followed by sonication in isopropyl alcohol for 20 minutes to clean the laser cut structure. A carbon-fiber rod (1 mm diameter, 55 mm height) was used as a whisker and glued on the top surface of the spring suspension. An N50 magnet with the same diameter and 2 mm height was glued on the bottom surface of the spring suspension. This assembly was placed on a 3D-printed structure which was designed to fixture the magnetic sensor (TLE493D-A2B6, Infineon) below the magnet (Figure 5). While this 3D-printed structure was made much larger than needed for testing, the active area of the sensor including the suspension was only 5.8 mm square.

D. Experimental Setup

A test setup (Figure 6) was constructed to measure the mechanical stiffness of the serpentine spring system and the B field response when the whisker was deflected. An angular displacement in the elevation angle (φ) was generated by pushing the whisker with a motorized stage (NRT 150, Thorlabs) and the reaction force at the pushing point was

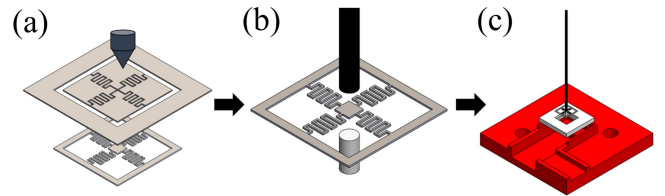


Fig. 5. Fabrication process of the whisker sensor: (a) UV laser cutting the steel sheet in a serpentine spring pattern, (b) attaching a carbon-fiber rod and cylindrical magnet, and (c) the sensor assembly mounted to the 3D printed fixture.

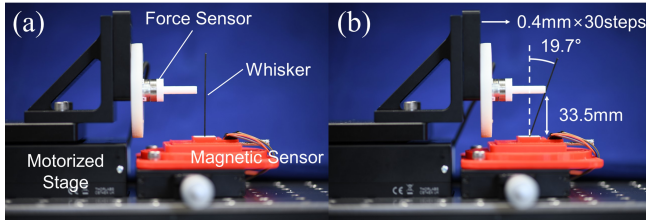


Fig. 6. Characterization setup for the whisker sensor with its whisker in (a) its neutral position, and (b) its fully displaced position

measured by an ATI Nano 17 Force/Torque Sensor. The TLE493D-A2B6 magnetic sensor from Infineon Technology was linked to a microcontroller (Arduino Due) through an I2C serial interface. All of the measurement devices and stages were connected and controlled via Matlab, which enabled the data acquisition process to be fully automated.

A step-wise displacement of 0.4 mm/step was applied over 30 steps at a fixed height of 33.5 mm relative to O (Figure 6(b)). This was equivalent to a total angular displacement of 19.7° , which is similar to the sensing range of real rat whiskers. The data acquisition protocol was designed to collect 20 data sets during each step, where a data set consisted of angular displacement, reaction force, and magnetic flux density readings. Identical experiments were conducted at 12 different azimuth angles (θ), with 30° steps. It is important to note that the TLE493D magnetic sensor was not calibrated for this study, and experimental results (especially linking magnetic field and angle) are therefore not expected to be a perfect match to the model. The sensitivity of this sensor, in particular, is listed as highly variable in the datasheet.

III. RESULTS

A. Serpentine Spring Characterization

1) *Spring fabrication result:* Figure 7(a) shows the fabricated dimensions of the serpentine springs. Laser cutting does not result in perfectly vertical sidewalls, and the bottom of the spring is wider than the top. To better characterize the resulting structure, a confocal microscope (Zeiss LSM800) was used to measure a 3D image of the spring (Figure 7(b)). The width of the spring at the top surface was thinner than the width at the bottom surface, demonstrating the slope of

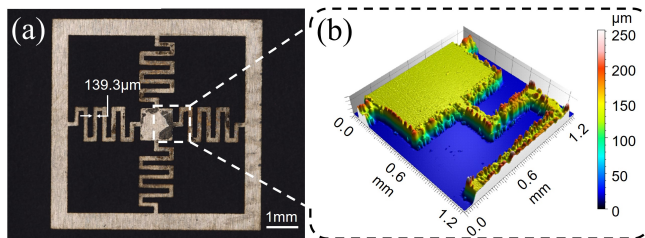


Fig. 7. Microscope images of the fabricated serpentine spring system. (a) Normal view from the bottom surface of the spring with dimensions, (b) 3D image showing sloped sidewalls in the serpentine spring captured with a confocal microscope

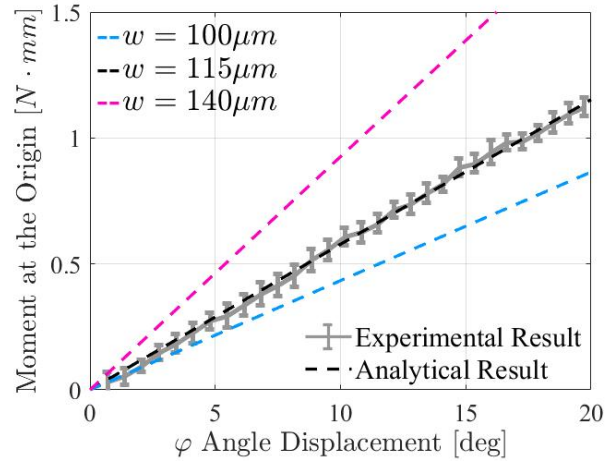


Fig. 8. Comparison of experimental and analytical results of the moment at the origin with variable elevation angle φ (fixed $\theta = 0^\circ$). Color represents differing spring width values for the analytical solution.

the laser-cut side walls. The width of the serpentine spring at the bottom surface was $139.3 \mu\text{m}$ while the original designed width was $100 \mu\text{m}$. The effective width of these beams is likely to fall in between these two numbers.

2) *Moment response:* The moment generated at the origin by the spring system is expected to be linearly proportional to the angular displacement. The result of the moment response (with fixed $\theta=0^\circ$) is plotted in grey with error bars in Figure 8. The analytical model of the spring system is plotted using two different widths – the designed width ($100 \mu\text{m}$) in blue and the approximate width of the spring's bottom surface ($140 \mu\text{m}$) in pink. The experimental result was stiffer than a spring with a width of $140 \mu\text{m}$, but less stiff than a spring with a width of $100 \mu\text{m}$. An equivalent spring width was calculated at $115 \mu\text{m}$ by manually fitting the analytical result to experimental result (black line). The moment increases linearly up to 1.1 Nmm when φ varies from 0° to 19.7° . The measured angular stiffness of the spring system for $\theta=0^\circ$ is therefore 3.20 Nmm/rad .

B. Magnetic Field Response

Figure 9 plots the change in B field with respect to θ when φ is fixed at 19.7° , the fully displaced state. This change is measured relative to the magnetic field when the whisker is in its undeflected state. The plot also shows the calculated results of the magnetic field analysis, which are represented by dashed lines. The analytical solution was plotted using the values in Table I, except for d_s (distance from magnet to sensing point) which was fit to 3.45 mm from the B_x and B_y data due to large uncertainty in this parameter from the experimental setup. When θ varied from 0° to 330° , ΔB_x and ΔB_y changed sinusoidally as expected from the analytical result. ΔB_z remained relatively constant as expected, but with slight variations likely due to misalignment between the magnet and the sensor. Unless the magnet is perfectly aligned over the magnetic sensor hidden in the package, some variation of ΔB_z with θ is expected.

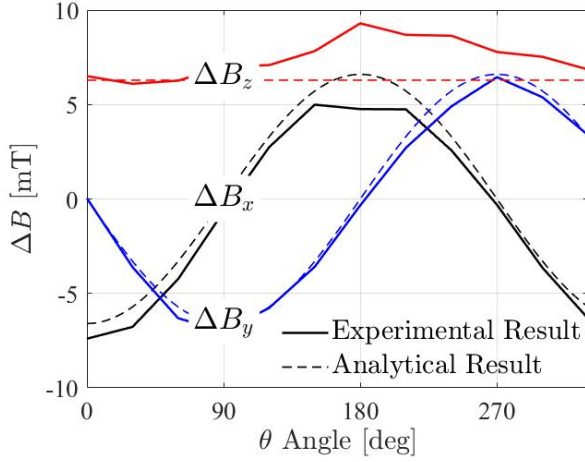


Fig. 9. Comparison between analytical and experimental results of the B field measured with variable azimuth angle θ (fixed $\varphi = 19.7^\circ$)

Figure 10 plots the change in B_z versus φ for a fixed azimuth angle ($\theta = 0^\circ$), showing a clear correlation between ΔB_z and φ . The error bars reflect the standard deviation of the 20 measurements taken at each step. Overall, the analytical result is a good predictor of the experimental result but the slopes of the two curves are slightly different. This is likely due to variation in the sensitivity of the 3D magnetic sensor. The nominal sensitivity (0.13 mT/LSB) was used to calculate ΔB_z , but the sensor datasheet specifies that this sensitivity can vary between 0.095 mT/LSB and 0.182 mT/LSB.

These experimental results can be used to calculate an approximate linear angular sensitivity of the whisker sensor (in $^\circ/\text{LSB}$) for changes in φ . The maximum angular displacement in Figure 10 is divided by the total change in B_z and multiplied by the sensitivity of the magnetic sensor

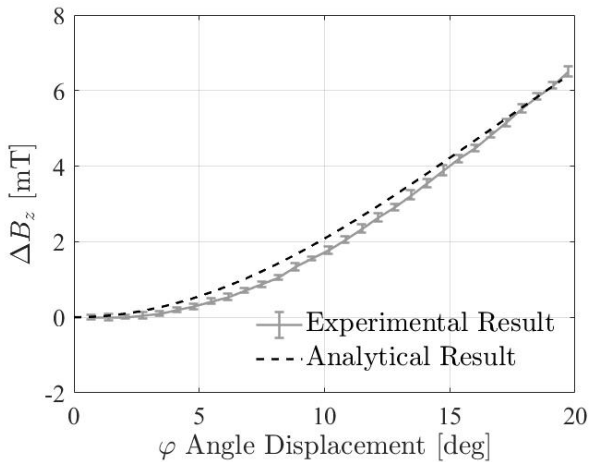


Fig. 10. Comparison between analytical and experimental results of the change in B_z measured over variable elevation angle φ (fixed $\theta = 0^\circ$). Error bars represent the standard deviations across the twenty measurements taken at each step.

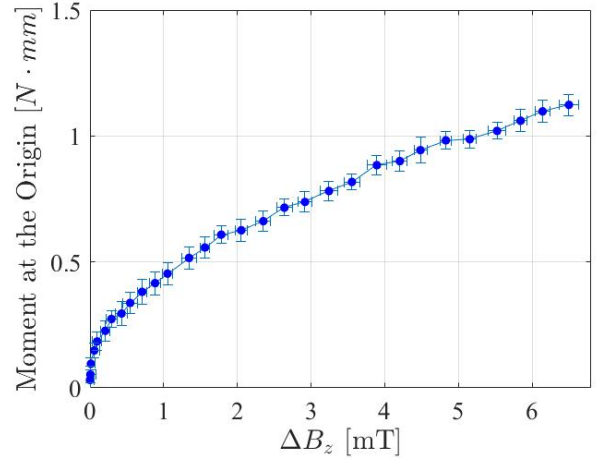


Fig. 11. Moment sensing characterization curve of ΔB_z to moment at origin (fixed $\theta = 0^\circ$)

(nominally 0.13 mT/LSB).

$$\frac{19.7^\circ}{6.8\text{mT}} \cdot 0.13\text{mT}/\text{LSB} = 0.38^\circ/\text{LSB}$$

In practice, noise from the sensor was on the order of 1-3 LSB, resulting in nominal whisker sensor resolution of 0.38° to 1.1° . Sensitivity in θ is more challenging to calculate; magnitudes of the sinusoids in Figure 9 will change based on the current φ and sensitivity will vary along with this. Sensitivity will be highest at large φ .

C. Moment Sensing

Ultimately, the goal is to calculate moment directly from the measured magnetic fields given the importance of knowing moments at the base of the whisker for calculating quantities like contact location in tactile sensing. The moment at the origin was linear with angular displacement in φ (Figure 8), which is correlated to ΔB_z (Figure 10). By plotting the relation between ΔB_z and the moment (Figure 11), the moment sensitivity of the system can be visualized and calculated. At small moments, ΔB_z does not change significantly, but this sensitivity increases at higher moments. Two sensitivities were calculated from Figure 11 assuming the same nominal magnetic sensor sensitivity of 0.13 mT/LSB: full-range and linear-range ($\Delta B_z > 1.8$ mT) sensitivity.

Full Range Sensitivity :

$$\frac{1.1\text{N} \cdot \text{mm}}{6.8\text{mT}} \cdot 0.13\text{mT}/\text{LSB} = 0.021\text{N} \cdot \text{mm}/\text{LSB}$$

Linear Range Sensitivity :

$$\frac{0.5\text{N} \cdot \text{mm}}{5\text{mT}} \cdot 0.13\text{mT}/\text{LSB} = 0.013\text{N} \cdot \text{mm}/\text{LSB}$$

Given maximum noise levels of 3 LSB, we expect a moment resolution of approximately 0.063 Nmm.

D. Calibration

While the analytical model provides a strong tool for whisker sensor design and is largely validated by the experiments above, it does not provide a perfect prediction of

angular deflections and bending moment in its current form due to fabrication tolerances and magnetic sensor tolerances. Instead, a calibration function was extracted using a Gaussian Process (GP) regression from the 360 sets of data acquired during experiments (30 φ angles \times 12 θ angles). Each data set included θ , φ , moment, and $\Delta \vec{B}$ ($= [\Delta B_x, \Delta B_y, \Delta B_z]$). The function input is $\Delta \vec{B}$, and the outputs are θ , φ , and moment. The calculation of all three outputs (θ , φ , and moment) from one $\Delta \vec{B}$ input took 2.5 ms of computing time using Matlab resulting in a maximum sampling/conversion rate of approximately 400 Hz for the whisker sensor.

IV. SYSTEM INTEGRATION

A. Graphical Interface

Figure 12 shows a graphical interface demonstrating simple measurements from the calibrated whisker sensor. The motion of the whisker was represented by the rotation of the black line in the screenshots, and the magnitude of the moment is presented and updated in the text. The update frequency of the graphic interface was 50 Hz. As seen in Figure 12(a), the noise in the whisker's neutral position is within the expected range calculated earlier. Figures 12(b-d) show that the interface is able to provide both bending moment and direction.

B. Contact Trajectory Sensing

While the whisker used in these tests was a rigid carbon fiber rod very unlike real whiskers (e.g., [16]), it can still be used to demonstrate simple capabilities and future directions for improved whisker sensors. In this test, the whisker base was moved forward at 5 mm s^{-1} on a linear stage while the whisker tip (in this case from a 71 mm whisker) came into contact with a 3D printed surface. The surface was designed to have both convex and concave regions. The angle φ calculated from the magnetic field measurements was then used to calculate the trajectory seen by the whisker tip in y and compared to the true trajectory defined by the surface.

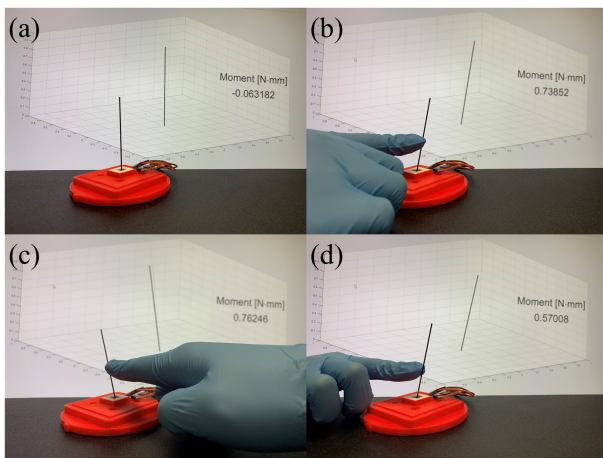


Fig. 12. Demonstration of a Matlab graphical interface for the whisker sensor, showing the response in (a) its neutral state, and variable φ deflection for (b) $\theta=0^\circ$, (c) $\theta=90^\circ$, and (d) $\theta=270^\circ$

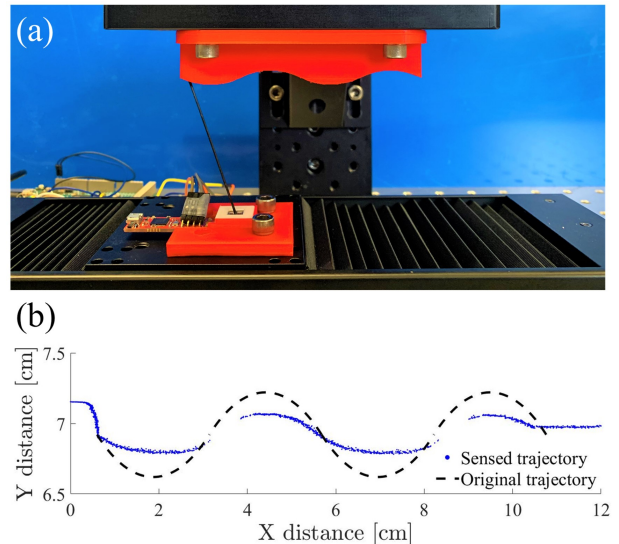


Fig. 13. (a) the experimental setup of the trajectory tracking test, and (b) the calculated results from that test included with the actual surface.

The results are shown in Figure 13 and a movie can be seen in the supplementary video. While the results are not perfect (primarily due to the rigid nature of the whisker), the test does demonstrate some basic tracking success, especially within the calibrated range for φ .

V. CONCLUSIONS

This work presented a novel magnetic transduction method for whisker sensing that enables low-cost, small, robust, and scalable whiskers that can measure applied moments at the base of the whisker. The sensor design is supported by an analytical model incorporating a model for the magnetic field from a cylindrical magnet along with the rotation of that magnet due to a moment applied to a compliant suspension. The sensor was characterized by applying known angular deflections to the whisker and measuring the corresponding moments and magnetic fields. The sensor was calibrated to provide applied moment and direction at the base of the whisker as well as the angular deflection of the whisker.

The measurement of moments is an important outcome of this work. When flexible and tapered whiskers are added in the future, measurement of these moments will help to detect contact location along with shapes and textures of nearby objects similar to work by [10]. The demonstrated trajectory tracking was a preliminary step in this direction. Larger arrays of whiskers can provide even more information. The fact that the transduction mechanism does not require electrical connection to the whisker means that the whisker is easily waterproofed for fluid flow sensing. The ability to quickly and inexpensively manufacture these sensors will ultimately improve the ability to include whiskers in a larger number of robotic systems.

APPENDIX

In this section, the magnetic field equation (f_B) in Eq (3) is re-stated in closed form [24] using the previously described

parameters.

$$\begin{aligned} B_x^{(M)} &= \frac{\mu_0 M_S R}{\pi} [\alpha_+ P_1(k_+) - \alpha_- P_1(k_-)] \cos \psi \\ B_y^{(M)} &= \frac{\mu_0 M_S R}{\pi} [\alpha_+ P_1(k_+) - \alpha_- P_1(k_-)] \sin \psi \\ B_z^{(M)} &= \frac{\mu_0 M_S R}{\pi(\rho + R)} [\beta_+ P_2(k_+) - \beta_- P_2(k_-)] \end{aligned}$$

μ_0 is the permeability of vacuum, and the auxiliary functions P_1 and P_2 are defined as,

$$\begin{aligned} P_1(k) &= \kappa - \frac{2}{1-k^2}(\kappa - \varepsilon) \\ P_2(k) &= -\frac{\gamma}{1-\gamma^2}(\varpi - \kappa) - \frac{1}{1-\gamma^2}(\gamma^2 \varpi - \kappa) \end{aligned}$$

The short-handed notations necessary to represent the intermediate steps of the calculation are shown below.

$$\begin{aligned} \xi_{\pm} &= Z_S \pm L, \quad \psi = \arctan(Y_S/X_S) \\ \alpha_{\pm} &= \frac{1}{\sqrt{\xi_{\pm}^2 + (\rho + R)^2}}, \quad \beta_{\pm} = \xi_{\pm} \alpha_{\pm} \\ \gamma &= \frac{\rho - R}{\rho + R}, \quad k_{\pm}^2 = \frac{\xi_{\pm}^2 + (\rho - R)^2}{\xi_{\pm}^2 + (\rho + R)^2} \end{aligned}$$

κ , ε , and ϖ are the evaluation of the complete elliptic integrals of the first, second, and third kind as described below.

$$\begin{aligned} \kappa &= K(\sqrt{1-k^2}) = \int_0^{\pi/2} \frac{d\theta}{\sqrt{1-(1-k^2)\sin^2\theta}} \\ \varepsilon &= E(\sqrt{1-k^2}) = \int_0^{\pi/2} d\theta \sqrt{1-(1-k^2)\sin^2\theta} \\ \varpi &= \Pi(1-\gamma^2, \sqrt{1-k^2}) \\ &= \int_0^{\pi/2} \frac{d\theta}{(1-(1-\gamma^2)\sin^2\theta)\sqrt{1-(1-k^2)\sin^2\theta}} \end{aligned}$$

ACKNOWLEDGMENT

This work was supported by the National Science Foundation award number BCS-1921251. The authors would also like to thank Tomas Debye and Alexander Olsen for early demonstrations using the magnetic field sensor, along with Prof. Mitra Hartmann for inspiration and feedback.

REFERENCES

- [1] R. A. Grant, S. Haidarliu, N. J. Kennerley, and T. J. Prescott, "The evolution of active vibrissal sensing in mammals: evidence from vibrissal musculature and function in the marsupial opossum *monodelphis domestica*," *Journal of Experimental Biology*, vol. 216, no. 18, pp. 3483–3494, 2013.
- [2] D. J. Krupa, M. S. Matell, A. J. Brisben, L. M. Oliveira, and M. A. Nicolelis, "Behavioral properties of the trigeminal somatosensory system in rats performing whisker-dependent tactile discriminations," *Journal of Neuroscience*, vol. 21, no. 15, pp. 5752–5763, 2001.
- [3] P. M. Knutsen, M. Pietr, and E. Ahissar, "Haptic object localization in the vibrissal system: behavior and performance," *Journal of Neuroscience*, vol. 26, no. 33, pp. 8451–8464, 2006.

- [4] D. H. O'Connor, N. G. Clack, D. Huber, T. Komiyama, E. W. Myers, and K. Svoboda, "Vibrissa-based object localization in head-fixed mice," *Journal of Neuroscience*, vol. 30, no. 5, pp. 1947–1967, 2010.
- [5] M. Brecht, B. Preilowski, and M. M. Merzenich, "Functional architecture of the mystacial vibrissae," *Behavioural brain research*, vol. 84, no. 1-2, pp. 81–97, 1997.
- [6] D. B. Polley, J. L. Rickert, and R. D. Frostig, "Whisker-based discrimination of object orientation determined with a rapid training paradigm," *Neurobiology of learning and memory*, vol. 83, no. 2, pp. 134–142, 2005.
- [7] Y. Boubenec, D. E. Shulz, and G. Debrégeas, "Whisker encoding of mechanical events during active tactile exploration," *Frontiers in behavioral neuroscience*, vol. 6, p. 74, 2012.
- [8] L. Miersch, W. Hanke, S. Wieskotten, F. Hanke, J. Oeffner, A. Leder, M. Brede, M. Witte, and G. Dehnhardt, "Flow sensing by pinniped whiskers," *Philosophical Transactions of the Royal Society B: Biological Sciences*, vol. 366, no. 1581, pp. 3077–3084, 2011.
- [9] N. Gläser, S. Wieskotten, C. Otter, G. Dehnhardt, and W. Hanke, "Hydrodynamic trail following in a california sea lion (*zalophus californianus*)," *Journal of Comparative Physiology A*, vol. 197, no. 2, pp. 141–151, 2011.
- [10] H. Emmett, M. Graff, and M. Hartmann, "A novel whisker sensor used for 3d contact point determination and contour extraction," *Proceedings of Robotics: Science and Systems, XIV*, 2018.
- [11] T. Assaf, E. D. Wilson, S. Anderson, P. Dean, J. Porrill, and M. J. Pearson, "Visual-tactile sensory map calibration of a biomimetic whiskered robot," in *2016 IEEE International Conference on Robotics and Automation (ICRA)*. IEEE, 2016, pp. 967–972.
- [12] C. W. Fox, M. H. Evans, M. J. Pearson, and T. J. Prescott, "Towards hierarchical blackboard mapping on a whiskered robot," *Robotics and Autonomous Systems*, vol. 60, no. 11, pp. 1356–1366, 2012.
- [13] M. H. Evans, C. W. Fox, N. F. Lepora, M. J. Pearson, J. C. Sullivan, and T. J. Prescott, "The effect of whisker movement on radial distance estimation: a case study in comparative robotics," *Frontiers in neurobotics*, vol. 6, p. 12, 2013.
- [14] N. F. Lepora, C. W. Fox, M. H. Evans, M. E. Diamond, K. Gurney, and T. J. Prescott, "Optimal decision-making in mammals: insights from a robot study of rodent texture discrimination," *Journal of The Royal Society Interface*, vol. 9, no. 72, pp. 1517–1528, 2012.
- [15] M. Szwed, K. Bagdasarian, B. Blumenfeld, O. Barak, D. Derdikman, and E. Ahissar, "Responses of trigeminal ganglion neurons to the radial distance of contact during active vibrissal touch," *Journal of Neurophysiology*, 2006.
- [16] L. A. Huet, J. W. Rudnicki, and M. J. Hartmann, "Tactile sensing with whiskers of various shapes: determining the three-dimensional location of object contact based on mechanical signals at the whisker base," *Soft robotics*, vol. 4, no. 2, pp. 88–102, 2017.
- [17] A. E. Yang and M. J. Hartmann, "Whisking kinematics enables object localization in head-centered coordinates based on tactile information from a single vibrissa," *Frontiers in behavioral neuroscience*, vol. 10, p. 145, 2016.
- [18] C. W. Fox, B. Mitchinson, M. J. Pearson, A. G. Pipe, and T. J. Prescott, "Contact type dependency of texture classification in a whiskered mobile robot," *Autonomous Robots*, vol. 26, no. 4, pp. 223–239, 2009.
- [19] C. L. Schroeder and M. J. Hartmann, "Sensory prediction on a whiskered robot: a tactile analogy to optical flow," *Frontiers in neurobotics*, vol. 6, p. 9, 2012.
- [20] G. R. Scholz and C. D. Rahn, "Profile sensing with an actuated whisker," *IEEE Transactions on Robotics and Automation*, vol. 20, no. 1, pp. 124–127, 2004.
- [21] T. N. Clements and C. D. Rahn, "Three-dimensional contact imaging with an actuated whisker," *IEEE Transactions on robotics*, vol. 22, no. 4, pp. 844–848, 2006.
- [22] T. Paulino, P. Ribeiro, M. Neto, S. Cardoso, A. Schmitz, J. Santos-Victor, A. Bernardino, and L. Jamone, "Low-cost 3-axis soft tactile sensors for the human-friendly robot vizzy," in *2017 IEEE International Conference on Robotics and Automation (ICRA)*. IEEE, 2017, pp. 966–971.
- [23] H.-M. Chou, M.-J. Lin, and R. Chen, "Fabrication and analysis of awl-shaped serpentine microsprings for large out-of-plane displacement," *Journal of Micromechanics and Microengineering*, vol. 25, no. 9, p. 095018, 2015.
- [24] N. Derby and S. Olbert, "Cylindrical magnets and ideal solenoids," *American Journal of Physics*, vol. 78, no. 3, pp. 229–235, 2010.